



Combined effects of anisotropy and tension–compression asymmetry on the torsional response of AZ31 Mg



Nitin Chandola^a, Ricardo A. Lebensohn^b, Oana Cazacu^{a,*}, Benoit Revil-Baudard^a, Raja K. Mishra^c, Frédéric Barlat^d

^a Department of Mechanical and Aerospace Engineering, University of Florida, REEF, Shalimar, FL 32579, USA

^b Materials Science and Technology Division, Los Alamos National Laboratory, Los Alamos, NM 87545, USA

^c General Motors Research and Development Center, 30500 Mound Road, Warren, MI 40890-9055, USA

^d Graduate Institute of Ferrous Technology, Pohang University of Science and Technology, Republic of Korea

ARTICLE INFO

Article history:

Received 14 June 2014

Received in revised form 30 December 2014

Available online 29 January 2015

Keywords:

Orthotropy

Strength differential effects

Twinning

Swift effects

Magnesium (AZ31)

ABSTRACT

In this paper it is demonstrated that only by accounting for the combined effects of anisotropy and tension–compression asymmetry at polycrystal level, it is possible to explain and accurately predict the room-temperature torsional response of a strongly textured AZ31 Mg material. This is shown by using two modeling frameworks, namely: a viscoplastic self-consistent (VPSC) polycrystal model, and a macroscopic plasticity model based on a yield criterion, developed by Cazacu et al. (2006), that accounts for both orthotropy and tension–compression asymmetry in plastic flow. It is shown that unlike Hill's (1948) criterion, the latter macroscopic criterion quantitatively predicts the experimental results, namely: that the sample with axial direction along the rolling direction contracts, while the sample with axial direction along the normal direction elongates. Moreover, it is demonstrated that these experimentally observed axial strain effects can be quantitatively predicted with the VPSC polycrystal model, only if both slip and twinning are considered operational at single crystal level. On the other hand, if it is assumed that the plastic deformation is fully accommodated by crystallographic slip, the axial strains predicted by VPSC are very close with that predicted with Hill (1948) criterion, which largely underestimates the measured axial strain in the rolling direction, and predicts zero axial strain in the normal direction.

© 2015 Elsevier Ltd. All rights reserved.

1. Introduction

The Swift effect refers to the occurrence of plastic axial strains in a metallic specimen when subjected to free-end torsion. This phenomenon was first experimentally observed by Swift (1947), who reported plastic elongation of cylindrical specimens (solid rods and tubes) made of different materials with cubic crystal structure (e.g. stainless steel, aluminum, brass). Swift (1947) conjectured that strain hardening is the cause for the development of axial effects under torsional loadings. As stated by the author himself, this explanation is largely speculative and was later invalidated by Billington, 1977a,b,c. Hill (1950) stated that if a material is isotropic the specimen should not change its length under torsion and that the Swift effect is the result of texture-induced anisotropy. This remains the prevalent view. Nowadays, it is

generally accepted that the development of axial strain under free-end torsion is due to texture-induced anisotropy.

Moreover, from a theoretical standpoint the Swift effect is mainly modeled in the framework of crystal plasticity, and the majority of studies are devoted to materials with cubic crystal structure for which it is assumed that the plastic deformation is fully accommodated by crystallographic slip. The homogenized response of the polycrystal is obtained using the upper-bound Taylor approximation (deformation gradient within each grain has a uniform value throughout the aggregate), or a viscoplastic self-consistent formulation (e.g. Lebensohn and Tome (1993)). For example, Toth et al. (1990) used a rate-sensitive Taylor-type crystal plasticity model to simulate length changes and the texture developed during unconstrained deformation of thin-walled tubes of pure copper. Axial effects were qualitatively predicted for very large shear strains, the simulations indicating a strong influence of the strain-rate sensitivity parameter involved in the description of the single crystal behavior. Habraken and Duchene (2004) and Duchene et al. (2007) have also confirmed the significant influence

* Corresponding author. Tel.: +1 850 833 9350; fax: +1 850 833 9366.

E-mail address: cazacu@reef.ufl.edu (O. Cazacu).

of this strain-rate sensitivity parameter on the magnitude of predicted axial strains in copper under free-end torsion. Nevertheless, the predicted axial strains largely underestimate the experimental ones. Some other studies have been devoted to modeling cyclic Swift effect at large strains using phenomenological models. Generally, yielding and hardening are considered anisotropic (see, for example, Kuroda (1999)) who used the orthotropic Hill's (1948) yield criterion in conjunction with anisotropic hardening).

Regarding polycrystalline materials with hexagonal closed packed (hcp) crystal structure, the past decade has witnessed a renewed interest in improving the fundamental understanding of their plastic behavior. In particular, a large number of experimental studies have been conducted on magnesium alloys in order to identify the crystallographic plastic deformation mechanisms at room temperature and their effects on the macroscopic response in uniaxial tension and compression, as well as in simple shear along different orientations (e.g. Barnett (2007a,b), Jiang et al. (2008), Khan et al. (2011), etc.). In comparison, there is little information concerning the mechanical behavior of Mg and its alloys in torsion. Free-end torsion tests at room temperature, 150, and 250 °C on solid bars of pure Mg and Mg alloy AZ71 with the axis along the rolling direction were reported by Beausir et al. (2009) and Biswas et al. (2013). While at room temperature both materials developed very little shear strain, at 250 °C the maximum plastic shear reached in the test was much larger (e.g. for the pure Mg $\gamma = 1.7$ as compared to ~ 0.2 at room temperature). For all temperatures, shortening of the specimens was observed. In the simulations presented using the viscoplastic self-consistent model and code VPSC (Lebensohn and Tome, 1993), deformation twinning was not considered. Very recently, Guo et al. (2013) reported room-temperature torsion tests on AZ31 Mg alloy cylindrical solid bars machined from a rolled plate with a very strong initial basal texture. Specimens with longitudinal axis oriented along the rolling direction, and the through-thickness (normal direction) of the plate were tested. It was found that while the sample with longitudinal axis along the rolling direction contracts, the sample with longitudinal axis along the normal direction elongates. The occurrence of axial strains under torsion were attributed to tensile twinning, which, in turn, induces texture evolution in the material. However, for an hcp titanium with basal texture, elongation of the specimens is observed irrespective of the orientation of the long axis of the specimen as evidenced by the analysis of tubes obtained by flow-forming (see Scutti (2001)).

In summary, initial anisotropy and texture-induced anisotropy associated to either slip or deformation twinning have been considered to be the only causes of Swift effect in polycrystalline metals. However, Billington (1977a,b,c) reported that there are metals with cubic crystal structure that display a significant Swift effect, but remain isotropic over the entire range of plastic deformation. Very recently, a new interpretation of the Swift phenomenon in isotropic materials was provided by Cazacu et al. (2013) for monotonic torsion and by Cazacu et al. (2014) for cyclic torsion using a macroscopic modeling framework. Moreover, analytical calculations using the isotropic form of Cazacu et al. (2006) criterion showed that the occurrence of axial strains in isotropic materials is related to a slight difference between the uniaxial yield in tension and compression of the given material. For initially anisotropic materials (e.g. Ti and Mg alloys), Revil-Baudard et al. (2014) demonstrated that the orthotropic form of Cazacu et al. (2006) criterion in conjunction with isotropic hardening explains and predicts the type (elongation or contraction) of the axial strains that develop. More specifically, if the uniaxial yield stress in tension is larger than that in compression, the specimen will contract when twisted, while, if the yield stress in uniaxial compression is larger than that in uniaxial tension, it will elongate.

This paper is devoted to the modeling of the torsional response of an orthotropic AZ31 Mg alloy. For this purpose two approaches will be considered: (i) the polycrystalline VPSC homogenization approach (Lebensohn and Tomé, 1993), and (ii) an elastic/plastic approach based on the orthotropic yield criterion form of Cazacu et al. (2006). For comparison purposes, Hill's (1948) orthotropic criterion will be also applied to the same material. These models are presented in Section 2. Mechanical tests data on polycrystalline AZ31 Mg reported in Khan et al. (2011) will be used for calibration of the material's parameters involved in the VPSC and the macroscopic models (see Section 3). Next, these models will be applied to the description of the torsional response of specimens cut from an AZ31 Mg plate reported in Guo et al., 2013 (see Section 4). It is to be noted that this plate is made of the same alloy (same composition) and similar initial texture as the AZ31 Mg sheet tested by Khan et al. (2011). Comparison between the prediction of axial strain vs. shear strain for torsion in the RD direction obtained using the VPSC model (with crystallographic twinning considered active), and the orthotropic form of Cazacu et al. (2006) yield criterion, in conjunction with appropriate evolution laws for the anisotropy coefficients and the strength differential parameter, and the experimental data from Guo et al. (2013) show that both the macroscopic and polycrystalline models capture the unusual behavior in torsion of Mg AZ31. Concluding remarks are presented in Section 5.

Regarding notations, vectors and tensors are denoted by bold-face characters. If \mathbf{A} and \mathbf{B} are second-order tensors, the contracted tensor product between such tensors is defined as: $\mathbf{A} : \mathbf{B} = A_{ij}B_{ij}$, $i, j = 1 \dots 3$; if \mathbf{u} and \mathbf{v} are two vectors, their dyadic product is the second rank tensor $(\mathbf{u} \otimes \mathbf{v})_{ij} = u_i v_j$.

2. Constitutive models

2.1. Polycrystal model

The VPSC model will be used to gain insights into the role of specific single-crystal plastic deformation mechanisms on the macroscopic response of AZ31 Mg. This model is only briefly presented in what follows (a detailed description can be found in the review article by Tomé and Lebensohn (2004)). The polycrystal is represented by a finite set of orientations, each one representing a given volume fraction chosen to reproduce the initial texture. The total deformation of the polycrystal is obtained by imposing successive strain increments and calculating the resulting strains in the grains. The grain reorientations associated with these plastic strains lead to texture evolution. A self-consistent approach is used to model the interaction of a grain with its surroundings. Each grain is treated as an anisotropic, viscoplastic, ellipsoidal inclusion embedded in a uniform matrix having the unknown properties (to be determined) of the polycrystal. Elastic deformations are neglected. Each deformation system (s) is characterized by a vector \mathbf{n}^s (normal to the slip or twinning plane) and a vector \mathbf{b}^s (Burgers vector or twinning shear direction). The local constitutive behavior (at the grain level) is described by:

$$\mathbf{d}^g = \sum_s \mathbf{m}^s \dot{\gamma}^s = \dot{\gamma}_0 \sum_s \mathbf{m}^s \left(\frac{\mathbf{m}^s : \boldsymbol{\sigma}^g}{\tau_c^s} \right)^n \times \text{sgn}(\mathbf{m}^s : \boldsymbol{\sigma}^g), \quad (1)$$

where $\mathbf{m}^s = \frac{1}{2}(\mathbf{b}^s \otimes \mathbf{n}^s + \mathbf{n}^s \otimes \mathbf{b}^s)$ and $\dot{\gamma}^s$ are the Schmid tensor and the shear rate of system (s), \mathbf{d}^g and $\boldsymbol{\sigma}^g$ are the local averages of the strain rate and stress fields in grain (g), $\dot{\gamma}_0$ is a reference shear rate and n is a rate sensitivity parameter. Eq. (1) expresses that the deformation rate is given by the sum over all the shear rates contributed by all systems. For both slip and twinning, the activation criterion is given by the expression in parenthesis, which

expresses that the activity on each deformation system (s) increases when the resolved shear on that system (given by $\mathbf{m}^s : \sigma^g$) approaches a threshold value τ_c^s . Strain-hardening is incorporated by allowing the threshold stress τ_c^s to evolve according to:

$$\tau_c^s = \tau_0^s + (\tau_1^s + \theta_1^s \Gamma)(1 - \exp(-\frac{\theta_0 \Gamma}{\tau_1^s})), \quad (2)$$

where τ_0^s , τ_1^s , θ_0^s and θ_1^s are constants, and $\Gamma = \sum_s \dot{\gamma}^s \Delta t$ is the accumulated shear in all active deformation systems. In addition, it is possible to incorporate self and latent hardening. More specifically, the increase in the threshold stress is calculated as:

$$\Delta \tau_0^{s(r)} = \frac{d\tau^{s(r)}}{d\Gamma^{(r)}} \sum_k h^{ss'} \dot{\gamma}^{s'(r)} \Delta t, \quad (3)$$

where the coefficients $h^{ss'}$ empirically account for the obstacles that new dislocations (or twins) associated with system s' create for the propagation of dislocations (or twins) on system s . Following the approach proposed by Van Houtte (1978), twinning is treated as a pseudo-slip mechanism. Specifically, it differs from slip in its directionality, which means that activation of twinning is allowed only if the resolved shear stress is positive. The twinning contribution to texture development is accounted for by means of the so-called Predominant Twin Reorientation (PTR) scheme (Tomé et al., 1991). In this scheme, the grains where twinning is most active are determined. The fixed number of orientations that represent the polycrystal is maintained throughout the deformation history. The volumetric effect of twinning reorientation on texture development is modeled by reorienting some of these grains completely into the orientation of their most active twinning systems.

2.2. Macroscopic elastic/plastic model based on Cazacu et al. (2006) yield criterion

To explain and model Swift effects in AZ31 Mg, an elastic–plastic modeling approach in the framework of the mathematical theory of plasticity is also considered. The yield condition is based on the orthotropic form of Cazacu et al. (2006) yield function. For comparison purposes, Hill (1948) criterion will also be applied. In both cases hardening is considered isotropic. The general form of the governing equations are first presented and followed by the specific expressions of these yield criteria.

Tensile strains and stresses are considered positive. The total rate of deformation \mathbf{D} is the sum of the elastic part ($\mathbf{D} - \mathbf{D}^p$), and the plastic part, \mathbf{D}^p . The elastic stress–strain relationship is given by

$$\dot{\boldsymbol{\sigma}} = \mathbf{C}^e : (\mathbf{D} - \mathbf{D}^p), \quad (4)$$

where $\dot{\boldsymbol{\sigma}}$ is the Green–Naghdi rate, which is an objective rate of the Cauchy stress tensor σ (see Green and Naghdi (1965), ABAQUS (2009)). In this work we assume linear-elastic isotropy, so with respect to any Cartesian coordinate system, \mathbf{C}^e is expressed as

$$\mathbf{C}_{ijkl}^e = 2G \delta_{ik} \delta_{jl} - \left(K - \frac{2}{3}G \right) \delta_{ij} \delta_{kl}. \quad (5)$$

where $i, j, k, l = 1 \dots 3$, δ_{ij} is the Kronecker delta tensor, and G and K are the shear and bulk moduli, respectively. The rate of deformation tensor is given by the associated flow rule:

$$\mathbf{D}^p = \dot{\lambda} \frac{\partial F}{\partial \boldsymbol{\sigma}}, \quad (6)$$

where F is the yield function and $\dot{\lambda} > 0$ is the plastic multiplier. Strain hardening is considered isotropic and governed by the accumulated plastic strain. Thus, the plastic potential F in Eq. (6) is of the general form:

$$F(\boldsymbol{\sigma}, \bar{\epsilon}^p) = \bar{\sigma}(\boldsymbol{\sigma}, \bar{\epsilon}^p) - Y(\bar{\epsilon}^p), \quad (7)$$

where $\bar{\sigma}$ is the effective stress associated with the given yield criterion, $\bar{\epsilon}^p$ is the equivalent plastic strain which is calculated based on the plastic work equivalence principle (i.e. it is the work-conjugate of $\bar{\sigma}$), while $Y = Y(\bar{\epsilon}^p)$ is the hardening law. Specifically, a Voce-type hardening law is considered:

$$Y(\bar{\epsilon}^p) = A_0 - A_1 \exp(-A_2 \bar{\epsilon}^p), \quad (8)$$

where A_0, A_1, A_2 are constants.

The effective stress $\bar{\sigma}$ associated with the orthotropic form of Cazacu et al. (2006) criterion is:

$$\bar{\sigma} = B [(|\Sigma_1| - k|\Sigma_1|)^a + (|\Sigma_2| - k|\Sigma_2|)^a + (|\Sigma_3| - k|\Sigma_3|)^a]^{1/a}, \quad (9)$$

where a is a homogeneity constant (usually, $a = 2$). In Eq. (9) $\Sigma_1, \Sigma_2, \Sigma_3$ are the principal values of the transformed stress Σ defined as:

$$\Sigma = \mathbf{C} : \boldsymbol{\sigma}', \quad (10)$$

where $\boldsymbol{\sigma}'$ is the deviator of the Cauchy stress tensor $\boldsymbol{\sigma}$, and \mathbf{C} is a fourth-order symmetric tensor characterizing the plastic anisotropy of the material. For example, in the coordinate system associated with the orthotropy axes ($\mathbf{x}, \mathbf{y}, \mathbf{z}$) (for a plate material these axes of symmetry are the rolling (RD), transverse (TD), and normal direction (ND) or through-thickness plate direction, respectively) the transformed stress tensor Σ is given by:

$$\begin{bmatrix} \Sigma_{xx} \\ \Sigma_{yy} \\ \Sigma_{zz} \\ \Sigma_{xy} \\ \Sigma_{yz} \\ \Sigma_{xz} \end{bmatrix} = \begin{bmatrix} C_{11} & C_{12} & C_{13} & 0 & 0 & 0 \\ C_{12} & C_{22} & C_{23} & 0 & 0 & 0 \\ C_{13} & C_{23} & C_{33} & 0 & 0 & 0 \\ 0 & 0 & 0 & C_{44} & 0 & 0 \\ 0 & 0 & 0 & 0 & C_{55} & 0 \\ 0 & 0 & 0 & 0 & 0 & C_{66} \end{bmatrix} \begin{bmatrix} \sigma'_{xx} \\ \sigma'_{yy} \\ \sigma'_{zz} \\ \sigma'_{xy} \\ \sigma'_{yz} \\ \sigma'_{xz} \end{bmatrix}. \quad (11)$$

In Eq. (9) B is a constant defined such that $\bar{\sigma}$ reduces to the tensile yield stress in the RD direction or \mathbf{x} , i.e.

$$B = 1 / [(|\Phi_1| - k\Phi_1)^a + (|\Phi_2| - k\Phi_2)^a + (|\Phi_3| - k\Phi_3)^a]^{1/a}, \quad (12)$$

where $\Phi_1 = (2C_{11} - C_{12} - C_{13})/3$, $\Phi_2 = (2C_{12} - C_{22} - C_{23})/3$; $\Phi_3 = (2C_{13} - C_{23} - C_{33})/3$.

If a material has the same response in uniaxial tension and uniaxial compression, the parameter k involved in the yield criterion given by Eq. (9) is automatically zero. If the material displays tension–compression asymmetry, this material parameter is different from zero (for more details, see Cazacu et al. (2006)).

The equivalent stress associated to Hill (1948) criterion is expressed as:

$$\bar{\sigma}_{Hill} = \sqrt{F(\sigma_{yy} - \sigma_{zz})^2 + G(\sigma_{zz} - \sigma_{xx})^2 + H(\sigma_{xx} - \sigma_{yy})^2 + 2L(\sigma_{yz}^2) + 2M(\sigma_{zx}^2) + 2N(\sigma_{xy}^2)}, \quad (13)$$

where F, G, H, L, M and N are material parameters (anisotropy coefficients).

3. Identification of the constitutive models for AZ31 Mg

3.1. Identification of material parameters of the VPSC model

The polycrystal model VPSC has been previously used to simulate the plastic deformation of AZ31 Mg at room temperature. The focus of these studies was on modeling the deformation behavior under uniaxial tension or compression (e.g. Proust et al. (2009), Wang et al. (2010), etc.). Concerning simulation of the shear response, most of the efforts have been focused on understanding and modeling the high-temperature behavior of Mg and its alloys. It was established that at high temperature twinning activity is negligible, the plastic deformation being accommodated by pyramidal $\langle a \rangle$ and pyramidal $\langle c+a \rangle$ slip (e.g. for simulation of pure

Mg, see Agnew et al. (2005); for pure Mg and AZ71 Mg, see Beausir et al. (2009)).

To the best of our knowledge, modeling of the microstructure evolution and its effects on the macroscopic stress–strain response in simple shear of AZ31 Mg at room temperature were not reported. As already mentioned, the identification of the material parameters of VPSC will be based on the room-temperature quasi-static mechanical test data (strain rate of 10^{-2} /s) reported by Khan et al. (2011) on polycrystalline AZ31 Mg (3 wt%Al, 1 wt%Zn, Mg bal.). These uniaxial tensile and compression tests data reported in Khan et al. (2011) on specimens cut along the RD, TD, and 45° to the rolling direction of the sheet, and in the through-thickness direction compression showed that the material is plastically orthotropic. Moreover, irrespective of the loading direction the material displays a very strong tension–compression asymmetry in the macroscopic stress–strain response (see also Fig. 2).

The strong difference between the yield in tension and compression at the onset of plastic deformation (0.002 strain) and the unusual hardening behavior in uniaxial compression in RD (S-shape sigmoidal appearance of the stress–strain curve, see also Fig. 2) was attributed to the occurrence of tensile twinning (similar data and interpretation of the results have been also reported by Lou et al., 2007). It is to be noted that in simple shear along RD, Khan et al. (2011) reported that the volume fraction of tensile twins at 20% equivalent strain is of 0.506. The shear specimen has a higher volume fraction of twins as compared to the tension specimens, but much lower than in compression (80% at the same level of equivalent plastic strain).

Since in a typical polycrystal plasticity simulation, the polycrystal is represented with a discrete set of grains, in order to correctly capture the initial texture of the material it is necessary to consider a sufficiently large number of grains. Thus, we used the entire EBSD scan ($784 \times 808 \mu\text{m}$ area) to generate 2762 weighted orientations. The corresponding initial texture used in the simulations (Fig. 1(b)) is similar to that reported by Khan et al. (Fig. 1(a)). Note that the material displays a strong basal texture with an almost equal fraction of grains having their c -axes slightly tilted away (around $\pm 30^\circ$) from the sheet normal towards +RD and –RD, respectively.

Based on the experimental evidence provided by Khan et al. (2011), it can be assumed that basal, prismatic, and pyramidal $\langle c+a \rangle$ slip systems as well as tensile twinning are potentially active. For these deformation systems, the set of material parameters that characterize the plastic deformation at grain level was obtained using a step-by-step procedure. Specifically, the parameters associated with basal and prismatic slip systems were identified based on the stress–strain mechanical response in uniaxial tension along RD. Next, using the uniaxial compression

stress–strain data in the ND direction, the parameters associated with the pyramidal $\langle c+a \rangle$ slip system were calibrated. Finally, from the uniaxial compression test along RD, the parameters associated to the tensile twinning system were determined. In addition to these four modes, the pyramidal $\langle a \rangle$ slip mode was also considered to be active in simple shear. The hardening parameters associated with this system were calibrated based on the reported shear stress vs. shear strain curve in the RD direction. The values of the parameters associated to all five deformation modes are given in Table 1. The reference shear rate, $\dot{\gamma}_0$, and the rate-sensitivity parameter n (see Eq. (1)) were prescribed to be the same for all deformation systems: $\dot{\gamma}_0 = 0.001 \text{ s}^{-1}$ and $n = 20$. The latent hardening coefficients h^{ss} (see Eq. (3)) associated with the interaction between basal slip and tensile twinning, and respectively non-basal $\langle a \rangle$ slip and tensile twinning were set to a value of 2. On the other hand, the hardening coefficient h^{ss} associated with interaction between pyramidal $\langle c+a \rangle$ slip and tensile twinning was set to unity in order to capture the very little twinning activity observed in ND compression.

Comparison between the polycrystalline model predictions of the stress–strain response in uniaxial tension and compression along the axes of orthotropy of the material (solid line) and all available data (symbols) are shown in Fig. 2. It can be concluded that the model describes very well both the strong anisotropy and the tension–compression asymmetry of the material for uniaxial loading in each orientation. To calibrate the parameters associated with the pyramidal $\langle a \rangle$ slip, we will use the shear stress–shear strain data in simple shear along RD (see Fig. 3). Predictions of the volume fraction of tensile twins and the texture evolution for the same test will serve for validation. If simple shear is applied in the $(x-y)$ plane (or (RD-TD) plane, in the positive RD (x direction) the only non-zero velocity component is $v_2 = \dot{\gamma}x$ (see also Fig. 3), so the imposed velocity gradient tensor \mathbf{L} are such that:

$$L_{21} = \dot{\gamma} \quad (14)$$

Simulation results are shown in Fig. 4. The calculations were terminated when the shear strain reached the value of $\gamma = 0.2$. All five deformation modes were considered to be active.

Fig. 4(a) shows a comparison between the predicted shear stress vs. shear strain response according to the polycrystal model (solid line), and mechanical data reported in Khan et al. (2011), along with the predicted textures corresponding to different levels of the shear strain, and the predicted evolution of the twin volume fraction (inset). Note that the VPSC model describes well the shear stress vs. shear strain response and predicts a final value of the twin volume fraction in agreement with that reported in Khan et al. (2011). The predicted relative slip/twinning activities are

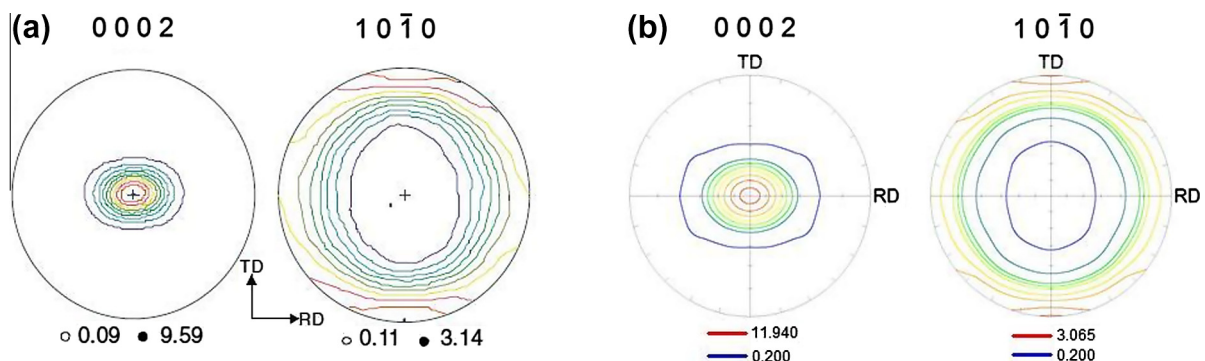


Fig. 1. Pole figures showing the initial texture of the AZ31 Mg sheet: (a) reported in Khan et al. (2011); (b) measured from the entire EBSD scan and used as input for the VPSC polycrystalline model.

Table 1
Material parameters involved in the hardening laws of various deformation modes for AZ31 Mg.

Mode	τ_0 [MPa]	τ_1 [MPa]	θ_0	θ_1
Basal $\{0001\}\langle 1\bar{2}10 \rangle$	17.5	5	3000	35
Prismatic $\{1\bar{1}00\}\langle 11\bar{2}0 \rangle$	85	33	550	70
Pyramidal $\langle a \rangle \{10\bar{1}1\}\langle \bar{1}2\bar{1}0 \rangle$	100	30	30	10
Pyramidal $\langle c+a \rangle \{10\bar{1}1\}\langle \bar{1}\bar{1}23 \rangle$	148	50	8500	0
Tensile Twinning $\{10\bar{1}2\}\langle \bar{1}101 \rangle$	52	0	0	0

shown in Fig. 4(b). The activity plot shows that tensile twinning activity is highest at approximately 0.05 von Mises equivalent strain ($\gamma/\sqrt{3}$). At this strain level, there is a slight kink in the macroscopic stress–strain response (Fig. 4(a)), indicating a change in the strain-hardening rate. It is important to note that the kink in the stress–strain curve was also observed experimentally at approximately 0.025 equivalent strain (see also Lou et al. (2007)), which was attributed to tensile twinning. Comparison between the only available measured texture and that predicted by the model is shown in Fig. 5. The final texture observed in

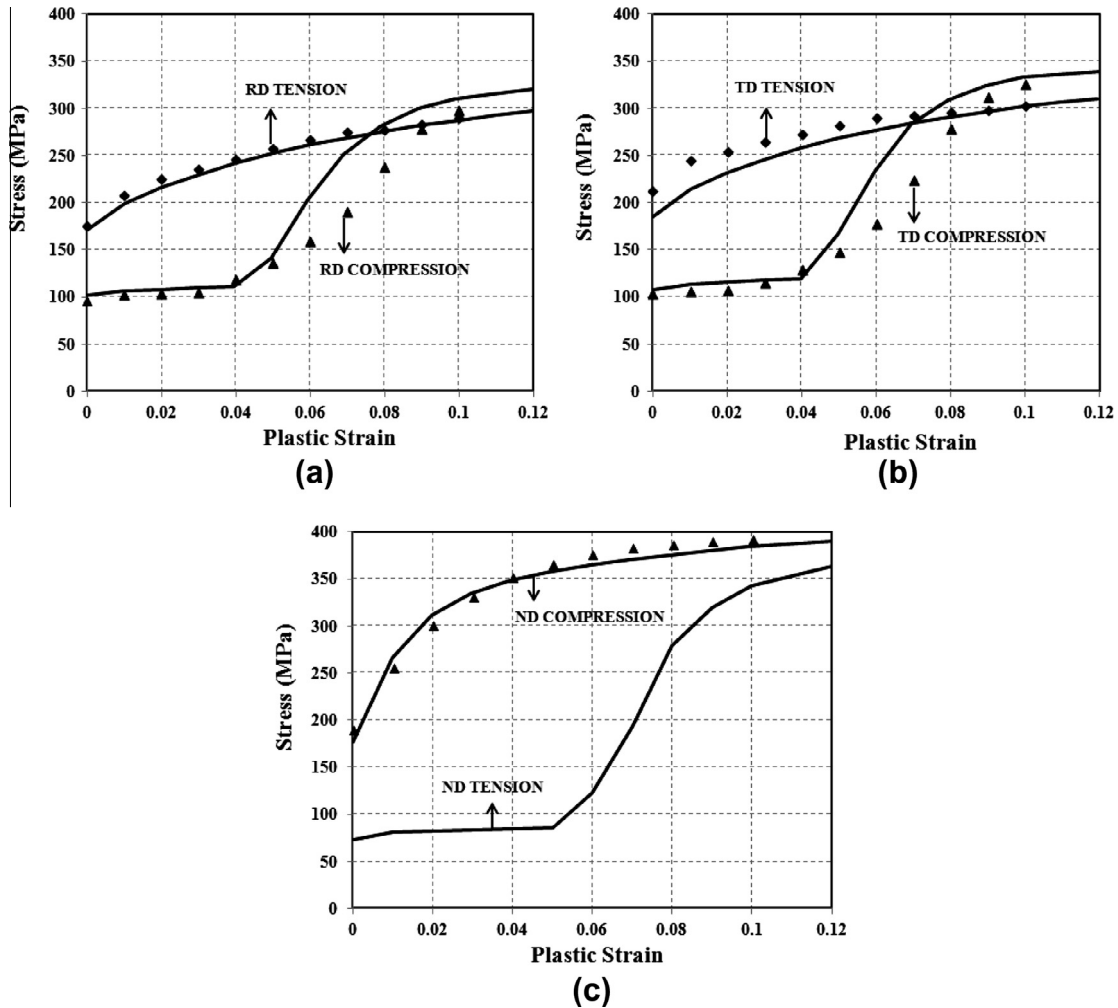


Fig. 2. Anisotropy of the stress–strain response in uniaxial tension and compression predicted with the VPSC model (lines) in comparison with data (symbols): (a) rolling direction (RD), (b) transverse direction (TD), and (c) normal direction (ND). Data after Khan et al. (2011).

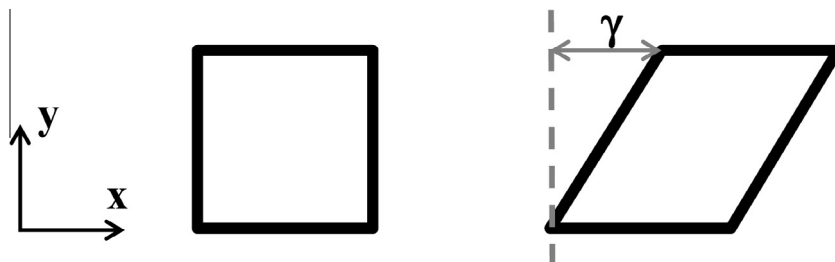


Fig. 3. Element subjected to a simple shear deformation γ in the plane $(x-y)$, x being along RD and y along TD.

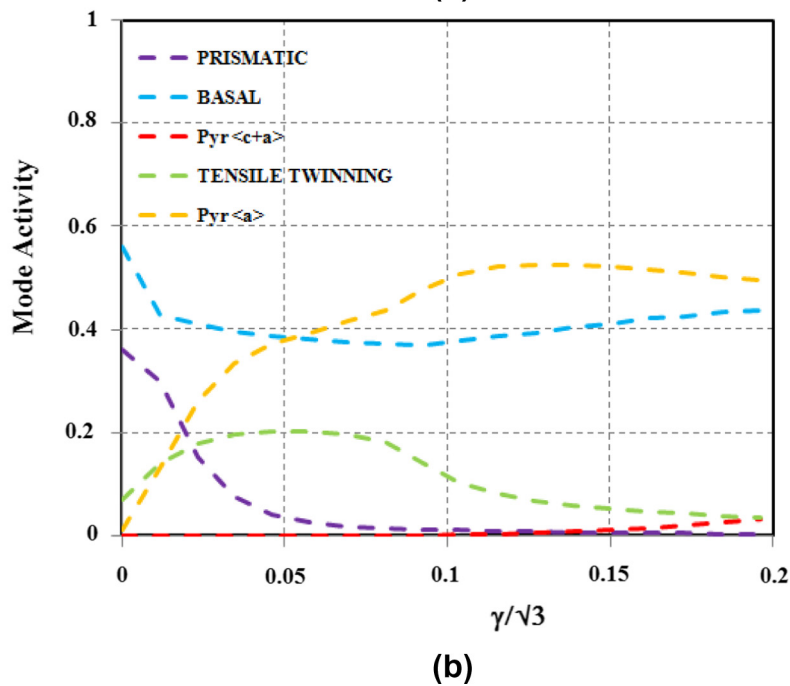
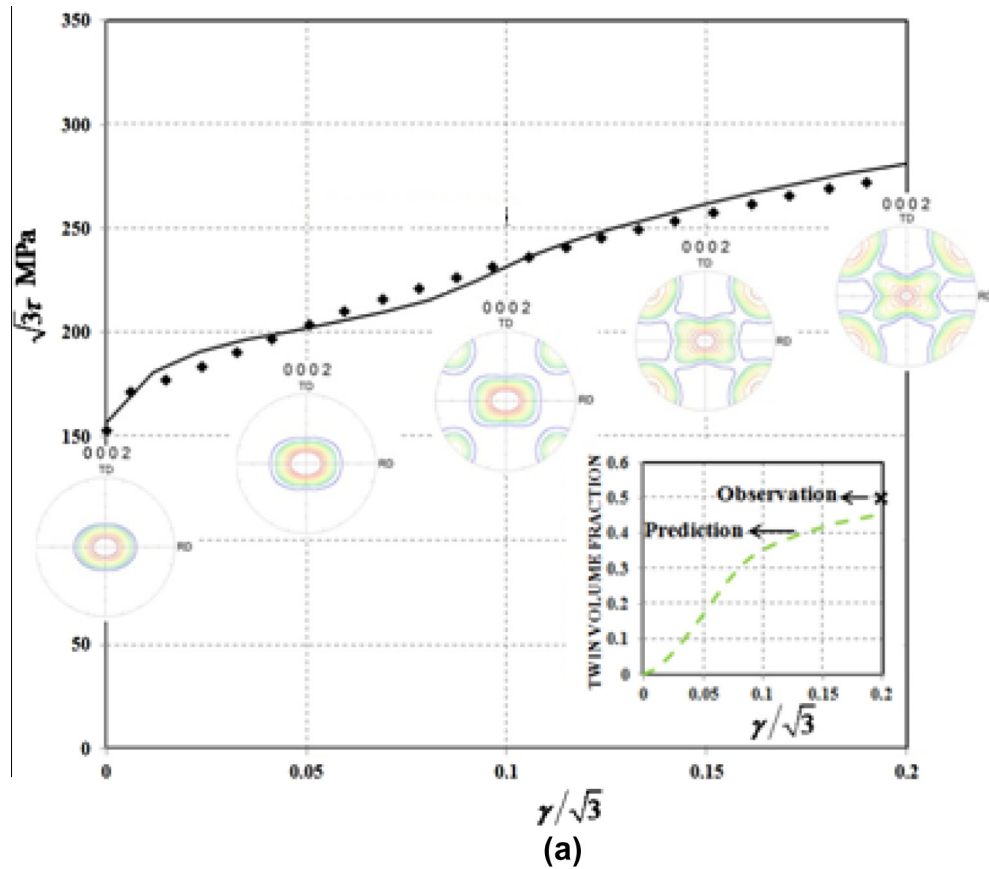


Fig. 4. (a) Predicted stress–strain, texture using the polycrystalline VPSC model for RD simple shear. Inset shows the predicted twin volume fraction evolution; and the only available experimental measurement (symbol) reported by Khan et al. (2011); (b) predicted relative activities of each deformation mode contributing to plastic deformation.

mechanical tests in RD simple shear is very close to that predicted by VPSC.

To gain understanding of the role played by individual plastic deformation mechanisms, two additional simulations were conducted. More specifically, simulation of the shear response was also done considering that plastic deformation is accommodated only by the four slip modes, i.e. neglecting tensile twinning

activity. The predicted macroscopic response and evolving microstructure is given in Fig. 6(a). It is worth noting that up to now in all the studies devoted to modeling the deformation response of AZ31 Mg using the VPSC model (Jain and Agnew, 2007; Wang et al., 2010; Guo et al., 2013) only basal, prismatic, and pyramidal $\langle c+a \rangle$ slip modes we considered active. However, pyramidal $\langle a \rangle$ slip mode appears to be necessary to explain microstructure

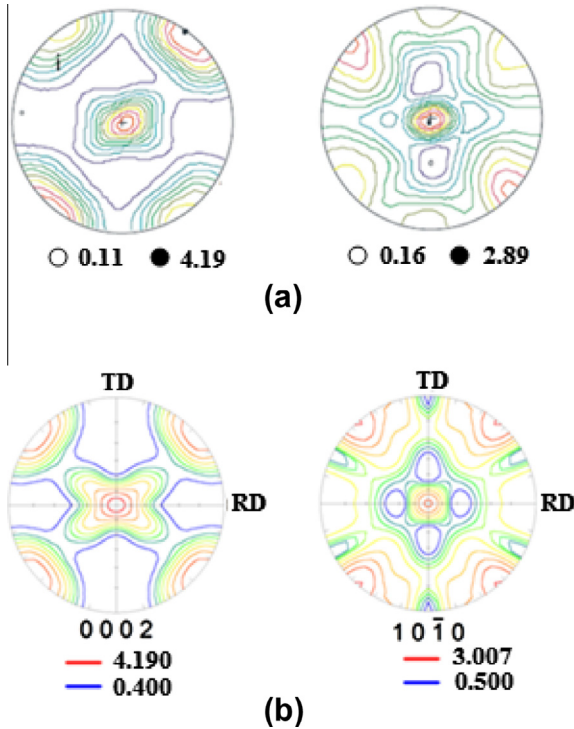


Fig. 5. Pole figures of AZ31 Mg sheet in RD simple shear test corresponding to a strain $\gamma/\sqrt{3} = 20\%$: (a) measured by Khan et al. (2011); (b) predicted by the VPSC model.

evolution in simple shear. In order to understand the role played by pyramidal $\langle a \rangle$ slip, simulation of the shear response was conducted considering that plastic deformation is accommodated by three slip systems, namely basal, prismatic, and pyramidal $\langle c + a \rangle$ slip (i.e. both pyramidal $\langle a \rangle$ slip and tensile twinning was neglected). The simulation results in comparison with available data are shown in Fig. 6(b). Note that if twinning activity is neglected, but all four slip models are considered active, the strains are slightly underestimated for $\gamma > 0.173$ (compare results in Fig. 6(a) with those in Fig. 4(a)); if both tensile twinning and pyramidal $\langle a \rangle$ slip are neglected, the strains are overestimated for the entire strain path history (compare results in Fig. 6(b) with those in Fig. 4(a)). While the results presented indicate that the

overall agreement between simulated and experimental shear stress vs. shear strain response is relatively good irrespective of which plastic deformation mechanisms are considered to be operational, it turns out that when twinning and pyramidal $\langle a \rangle$ slip are neglected, texture evolution is not correctly captured (compare texture evolution predicted in each case, i.e. Fig 4(a) with Fig. 6).

To further demonstrate this point, the experimental and predicted final textures in each case are compared in Fig. 7. Indeed, when tensile twinning and all the four slip modes (basal, prismatic, pyramidal $\langle a \rangle$ and pyramidal $\langle c + a \rangle$ slip) are considered active, the final observed and predicted textures match extremely well. However, if twinning is not operating, it is predicted that only a rotation of the initial texture occurs when the material is subjected to simple shear. More specifically, the polycrystal model predicts that the basal pole intensity is elongated 45° away from the shear direction (which is the RD direction), and the experimentally observed rotation of the $\langle c \rangle$ -axes is not captured at all. Furthermore, comparison between Fig. 7(c) and (d), shows the specific role played by pyramidal $\langle a \rangle$ slip, i.e. inhibiting the rotation of the basal planes along the two mutually perpendicular directions at 45° to RD.

3.2. Identification of the material parameters involved in the orthotropic yield criteria

As already mentioned, Cazacu et al. (2006) criterion (see Eq. (9)) accounts for both anisotropy and strength differential effects (tension–compression asymmetry). To identify the material parameters used in this criterion, only the mechanical tests in uniaxial tension and compression reported in Khan et al. (2011) were used. To model the difference in hardening rates between tension and compression loadings observed experimentally, the respective material parameters were considered to evolve with the accumulated plastic deformation. The numerical values of the model parameters corresponding to $\bar{\epsilon} = 0.05$ and three other individual levels of equivalent plastic strains (up to 0.1 strain) are listed in Table 2, the values corresponding to any given level of plastic strain $\bar{\epsilon}_p^j \leq \bar{\epsilon} \leq \bar{\epsilon}_p^{j+1}$ are obtained by linear interpolation, i.e.:

$$C_{ij}(\bar{\epsilon}) = \alpha(\bar{\epsilon})C_{ij}(\bar{\epsilon}_p^j) + (1 - \alpha(\bar{\epsilon}))C_{ij}(\bar{\epsilon}_p^{j+1})$$

$$k(\bar{\epsilon}) = \alpha(\bar{\epsilon})k(\bar{\epsilon}_p^j) + (1 - \alpha(\bar{\epsilon}))k(\bar{\epsilon}_p^{j+1}).$$
(15)

The interpolation parameter α involved in Eq. (15) is defined as:

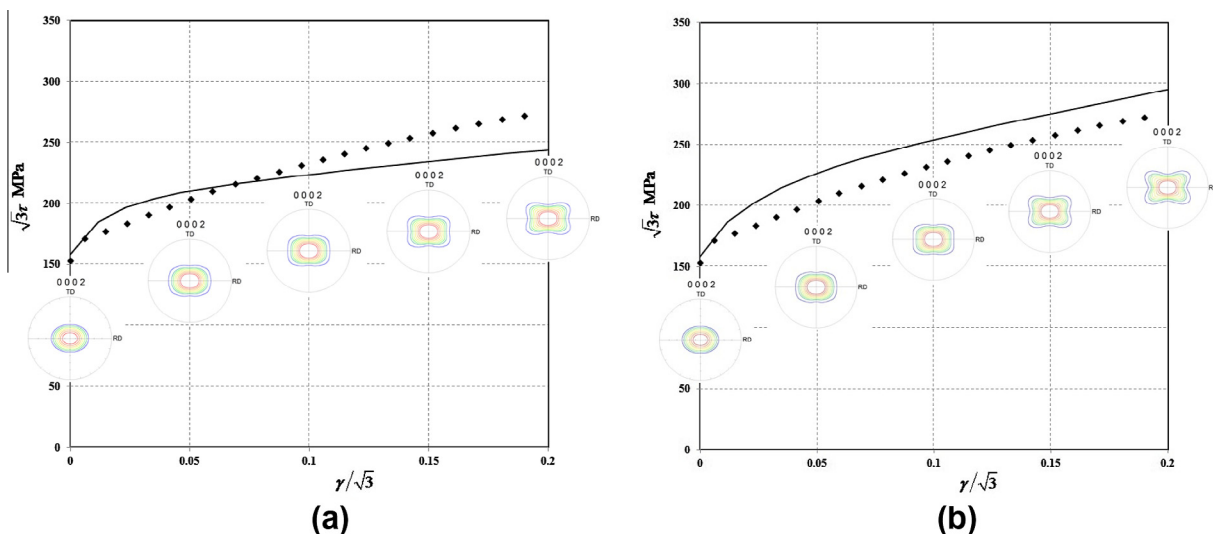


Fig. 6. Predicted effective stress vs. effective strain response and evolution of the microstructure in RD simple shear using the VPSC model (solid line): (a) all slip modes considered active, twinning neglected; (b) three slip modes considered active while pyramidal $\langle a \rangle$ and tensile twinning neglected.

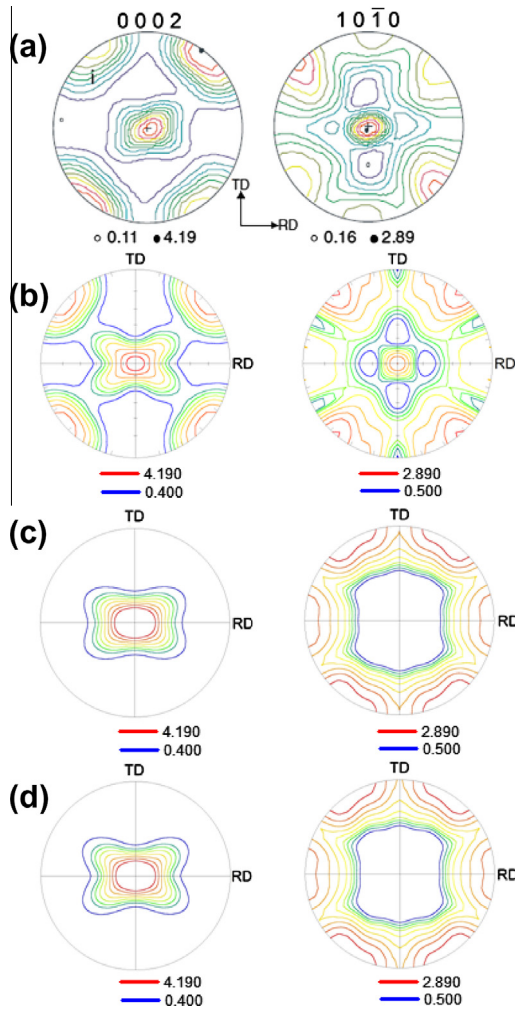


Fig. 7. Texture in simple shear corresponding to a strain $\gamma/\sqrt{3} = 20\%$ along RD direction obtained from: (a) experiments; (b) VPSC model predictions assuming that all four slip modes and tensile twinning active; (c) VPSC model predictions assuming that all slip modes are active and tensile twinning neglected; (d) VPSC predictions assuming that only three slip modes active, i.e. pyramidal (a) slip and tensile twinning neglected.

$$\alpha = \frac{\bar{\epsilon} - \bar{\epsilon}_p^j}{\bar{\epsilon}_p^{j+1} - \bar{\epsilon}_p^j} \quad (16)$$

Fig. 8 shows the projection in the biaxial plane (σ_{xx}, σ_{yy}), with \mathbf{x} being along RD and \mathbf{y} being along TD, of the theoretical yield surfaces according to the orthotropic Cazacu et al. (2006) at different strain levels $\bar{\epsilon}_p^j$, (up to 10%) along with the experimental data (symbols) for the given orthotropic AZ31 Mg alloy. The model correctly predicts that at initial yielding and below 8% strain, the tension–compression asymmetry is very pronounced (compare the tension–tension and compression–compression quadrants) while, for 8% strain and beyond, the difference in response between tension and compression becomes small, as observed experimentally (see also the experimental stress–strain curves of Fig. 2).

Table 2

Material parameters (orthotropy coefficients C_{ij} and strength-differential parameter k) involved in Cazacu et al. (2006) yield criterion for AZ31 Mg alloy corresponding to different values of plastic strain, $\bar{\epsilon}_p^j$; for any strain level C_{11} is set to unity.

$\bar{\epsilon}_p$	C_{22}	C_{33}	C_{12}	C_{13}	C_{23}	C_{44}	C_{55}	C_{66}	k
0.05	1.090	3.342	−0.168	0.098	0.243	0.730	7.30	7.74	−0.625
0.06	1.072	2.905	−0.595	−0.279	−0.096	1.039	10.2	11.02	−0.520
0.08	1.099	1.439	−0.817	−0.516	−0.350	1.128	11.21	11.95	−0.215
0.10	1.082	0.885	−0.762	−0.657	−0.509	1.058	10.12	11.21	−0.169

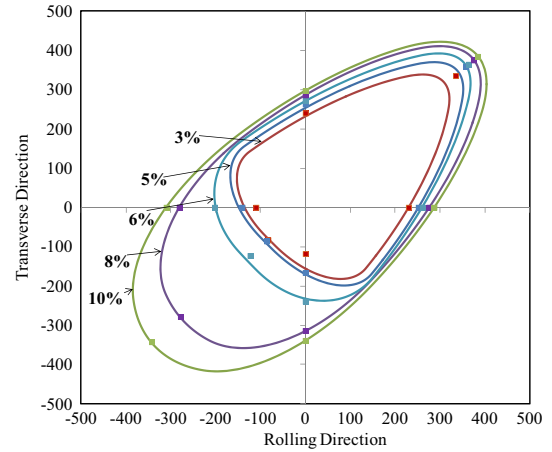


Fig. 8. Comparison between the theoretical yield surfaces, according to the orthotropic Cazacu et al. (2006) criterion, corresponding to different levels of accumulated plastic strain and data for an AZ31 Mg alloy. Note that the shape of the yield locus evolves from a triangle at lower strains to an ellipse at larger strains. Stresses are in MPa. Data from Khan et al. (2011).

Table 3

Orthotropy coefficients involved in Hill's (1948) yield criterion (Eq. (13)) for AZ31 magnesium alloy corresponding to different values of plastic strain.

$\bar{\epsilon}_p$	F	G	H	N	M	L
0.03	0.195	0.276	0.724	2.09	11.186	12.43
0.05	0.206	0.288	0.712	2.167	11.813	15.245
0.06	0.217	0.297	0.703	2.184	12.184	15.873
0.08	0.228	0.298	0.702	2.165	12.210	16.136
0.10	0.246	0.312	0.688	2.167	11.816	15.725

Since according to Hill (1948) criterion the mechanical response is the same in tension and compression, only the experimental flow stress data in uniaxial tension were used for the identification of the material parameters. The numerical values of all the anisotropy coefficients involved in Hill (1948) criterion (see Eq. (13)) are given in Table 3.

The yield surfaces associated with Hill (1948) yield criterion corresponding to different levels of equivalent plastic strains are plotted in Fig. 9. Note that the shape of Hill's (1948) yield surface is always elliptical and does not capture the tension–compression asymmetry of the material.

The parameters involved in the isotropic hardening law (Eq. (8)) that will be used in conjunction with each yield criterion were identified from the uniaxial tension stress–strain response along RD, the numerical values being $A_0 = 315.4$ MPa, $A_1 = 140.6$ MPa, $A_2 = 16.3$.

4. Prediction of the mechanical response of AZ31 Mg in free-end torsion

4.1. Simulation of free-end torsion of AZ31 Mg in the framework of crystal plasticity

It is to be noted that all the parameters involved in the VPSC crystal plasticity model (CRSS, and hardening coefficients, see

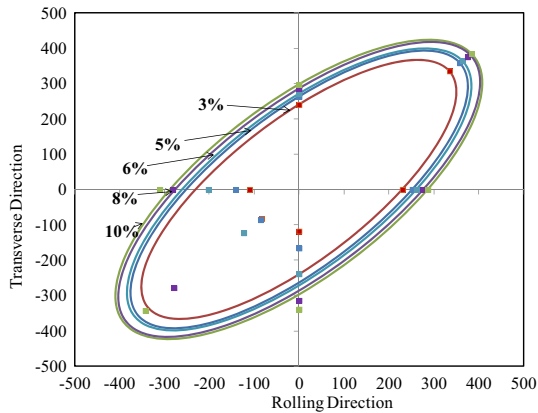


Fig. 9. Yield surfaces of AZ31 Mg corresponding to fixed levels of accumulated plastic strain according to Hill (1948) orthotropic criterion against mechanical test data (symbols). Stresses are in MPa. Data from Khan et al. (2011).

Table 1), characterize single-crystal deformation mechanisms. It is expected that the VPSC model can be further used to predict the polycrystalline response of an AZ31 Mg of similar initial texture (strongly basal). The AZ31 Mg plate material tested by Guo et al. (2013) has the same chemical composition, and a strongly basal initial texture similar to that of the AZ31 Mg sheet used for calibration of the model parameters. In the following, we will apply the VPSC model with the values of the parameters given in Table 1 to simulate the torsional response of specimens with long axis either along RD or ND, reported by Guo et al. (2013).

For the simulations using VPSC, we make the usual hypothesis that locally the state of deformation is that of simple shear (see Beausir et al. (2009)). It is also to be noted that this approximation is generally made by experimentalists when analyzing torsion test data (e.g. Holtom et al. (2013)). Fig. 10 shows a comparison between the axial strain vs. shear strain predicted by the VPSC model and data for the RD specimen. It is important to note that irrespective of the deformation modes that are considered to be active, shortening (i.e. axial strains negative) of the specimen along the direction of twist is qualitatively predicted. However, only in the case when tensile twinning is considered active, there is quantitative agreement with the data, in particular the slope of the experimental curve is correctly predicted. Fig. 11 shows a comparison between the axial strain vs. shear strain predicted by the VPSC model for both the RD and ND specimens. For the simulations presented in this figure it was assumed that tensile twinning and all four slip modes are active. Note that the polycrystalline model predicts correctly the nature of axial strains that develop, i.e. that in ND torsion the axial strains are positive (elongation of the sample) while the RD specimen shortens (axial strains negative).

4.2. FE simulation of the torsional response of AZ31 Mg using the macroscopic models

For anisotropic materials, the boundary value problem associated to torsional loading cannot be solved analytically. Hence, it was solved numerically using the finite-element (FE) method. All the simulations were carried out with the commercial FE code ABAQUS, using user material routines (UMAT) that we developed for the anisotropic elastic–plastic model with yielding described by Cazacu et al. (2006) criterion and Hill (1948) criterion, respectively. A fully implicit integration algorithm was used for solving the governing equations. The geometry of the specimen and FE mesh used in all the calculations is shown in Fig. 12. The FE mesh consists of 1290 hexahedral elements with reduced integration (ABAQUS C3D8R). The initial minimal section was meshed with

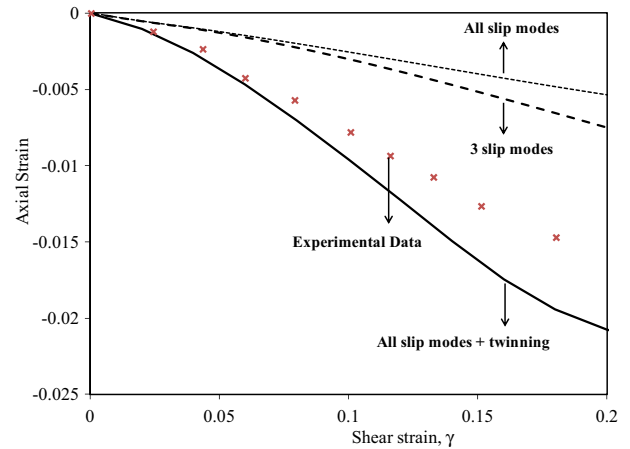


Fig. 10. Comparison of the axial strain vs. shear strain curve according to the VPSC model (lines) and that observed experimentally (symbols) for free-end torsion of AZ31 Mg alloy of a specimen with axis along RD. Data from Guo et al. (2013).

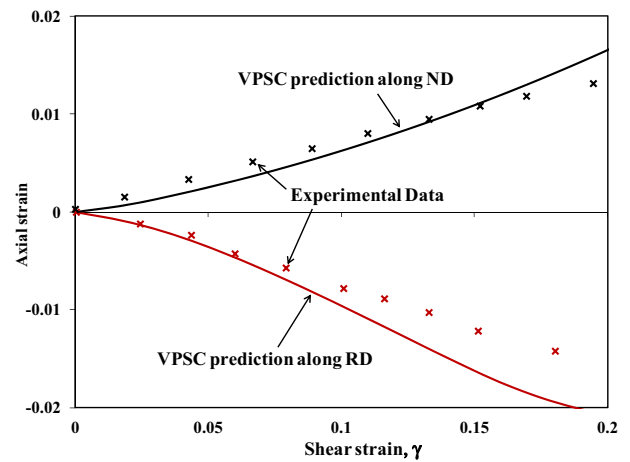


Fig. 11. Comparison between the experimental variation and VPSC predictions of the axial strain vs. shear strain for free-end torsion of AZ31 Mg specimens with axis along RD and ND directions. VPSC predictions are obtained assuming that all slip modes and tensile twinning are initially active. Data from Guo et al. (2013).

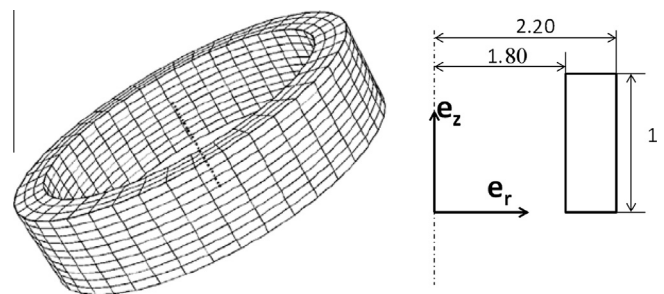


Fig. 12. Sample geometry and dimensions (mm) and finite-element mesh.

10 layers of elements. Three elements were used in the thickness of the specimen such as to reproduce as closely as possible the boundary conditions corresponding to the simulations using the VPSC model. The usual definitions of the axial and shear strains are used, namely:

$$\varepsilon = \ln \left(1 + \frac{u}{L_0} \right) \quad \text{and} \quad \gamma = \frac{\Phi r}{L_0}, \quad (17)$$

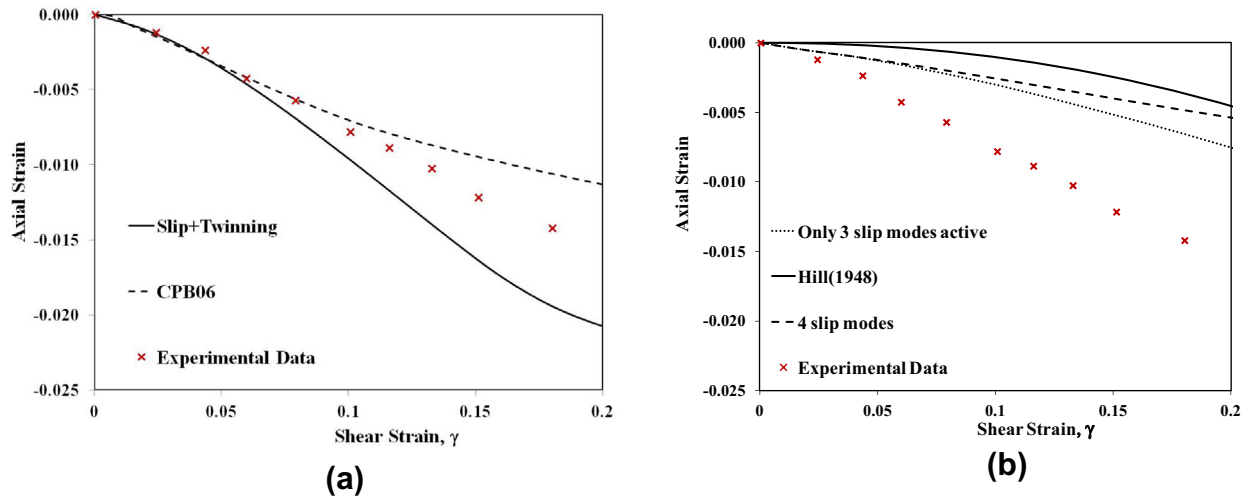


Fig. 13. Comparison between the experimental variation of the axial strain with the shear strain (symbols) during free-end torsion of an AZ31 Mg specimen with axis along RD and the predictions: (a) according to the orthotropic [Cazacu et al. \(2006\)](#) criterion and the VPSC model assuming that all slip modes and twinning are active; (b) according to the orthotropic [Hill's \(1948\)](#) criterion, and the VPSC model assuming that only slip modes are active and twinning neglected. Data from [Guo et al. \(2013\)](#).

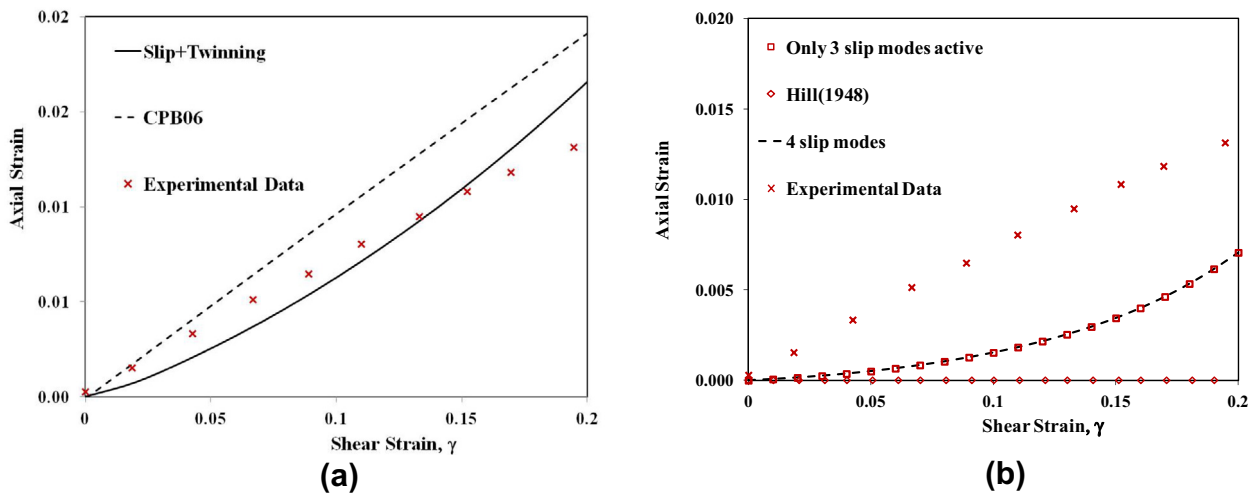


Fig. 14. Comparison between the experimental variation of the axial strain with the shear strain (symbols) during free-end torsion of an AZ31 Mg specimen with axis along ND and the predictions: (a) according to the orthotropic [Cazacu et al. \(2006\)](#) criterion and the VPSC model assuming that all slip modes and twinning are active; (b) according to the orthotropic [Hill's \(1948\)](#) criterion, and the VPSC model assuming that only slip modes are active and twinning neglected. Note that [Hill's \(1948\)](#) criterion predicts no axial strain. Data from [Guo et al. \(2013\)](#).

where r is the current radius, L_0 is the initial length, u is the axial displacement, and Φ is the twist angle. The lower nodes ($z = 0$) were pinned, i.e., no displacement was allowed, while the upper nodes ($z = L_0$) were tied to a rigid tool. Torsion was imposed by the rotation of this tool around the tube axis. The use of a rigid tool ensured that all the upper nodes experience the same boundary conditions. Note that the rigid tool allows free displacement along the specimen axis while all the other displacements (i.e. in plane displacements) and rotations were constrained.

Between five and six iterations per increment were necessary for convergence in the return mapping algorithm, the tolerance in satisfying the yield criterion being 10^{-7} (0.1 Pa). The Young modulus and Poisson coefficient used are: $E = 45$ GPa and $\nu = 0.3$, respectively.

Comparisons between FE simulations using the macroscopic models with yielding according to [Cazacu et al. \(2006\)](#) criterion and [Hill \(1948\)](#) criterion in conjunction with the isotropic hardening law of Eq. (8), and the data for Mg AZ31 under free-end torsion along the RD are presented in [Fig. 13](#). Note that all models predict

that the specimen contracts axially in the RD direction. However, only using [Cazacu et al. \(2006\)](#) criterion (which accounts for anisotropy and tension–compression asymmetry in yielding) both the level of axial strains and the slope of the axial vs. shear strain curve are accurately predicted (see [Fig. 13\(a\)](#)). On the other hand, [Hill \(1948\)](#) criterion largely underestimates the axial strains that develop in RD (see [Fig. 13\(b\)](#)).

It is worth noting that the predictions according to [Cazacu et al. \(2006\)](#) criterion are very close to these obtained using the VPSC polycrystal model when all slip modes and tensile twinning are considered operational (see [Fig. 13\(a\)](#)). However, the axial effects predicted by [Hill's \(1948\)](#) are very close with the VPSC polycrystal model predictions obtained when twinning activity is neglected (see [Fig. 13\(b\)](#)). Comparisons between FE simulations using the macroscopic models with yielding according to [Cazacu et al. \(2006\)](#) criterion and [Hill \(1948\)](#) criterion in conjunction with the isotropic hardening law of Eq. (8), and the data for Mg AZ31 under free-end torsion along ND are presented in [Fig. 14](#). It is very important to note that while [Cazacu et al. \(2006\)](#) criterion describes the

elongation of the specimen observed experimentally (see Fig. 14(a)), Hill (1948) criterion cannot capture any Swift effects in ND torsion (see Fig. 14(b)). In summary, these results show for the first time that unless tension–compression asymmetry in plastic flow is captured at every scale, the peculiarities of the torsional response of polycrystalline Mg AZ31 cannot be predicted. It was also demonstrated that only by considering that all slip modes (basal, prismatic and pyramidal $\langle c + a \rangle$, and pyramidal $\langle a \rangle$) and tensile twinning are active, both the mechanical behavior and the microstructure evolution of the Mg AZ31 alloy in shear can be predicted with accuracy using VPSC.

5. Conclusions

In this paper, the understanding of Swift effect in Mg AZ31 has been improved at different scales, using both a macroscopic plasticity and a crystal plasticity approach. Independent of the modeling framework used, it was shown that Swift effects in AZ31 Mg are due to the combined effects of anisotropy and tension–compression asymmetry: Only if a macroscopic criterion that accounts for both tension–compression asymmetry and anisotropy is used, Swift effects can be predicted in both RD and ND directions. Likewise, only if tensile twinning and all four slip modes are considered operational at single-crystal level, Swift effects in both orientations can be captured. Specifically, comparison between the prediction of axial strain vs. shear strain for torsion in the RD direction obtained using the VPSC model (with twinning considered active), and Cazacu et al. (2006) yield criterion, and experimental data show that both models capture the experimental trends irrespective of the twist axis. Moreover, the predictions of the initial slopes of the axial strain vs. shear strain curves obtained with the macroscopic model and the VPSC model are very close and in quantitative agreement with the experimental data. Even at large shear strains, e.g. at $\gamma = 0.2$, both the VPSC model with twinning operational and Cazacu et al. (2006) macroscopic model provide significant improvement over existing models. In RD, the difference between the latter models prediction and data is of 25% while the difference between data and the predictions of Hill (1948) and VPSC model with twinning neglected (only slip systems operational) is larger than 60%. In ND direction, Hill (1948) predicts zero strains while VPSC model (only slip systems operational) largely under-predicts axial effects.

References

- ABAQUS, 2009. User's Manual for Version 6.8, vols. I–V. Dassault Systemes Simulia Corp., Providence, RI.
- Agnew, S.R., Duygulu, O., 2005. Plastic anisotropy and the role of non-basal slip in magnesium alloy AZ31B. *Int. J. Plast.* 21, 1161–1193.
- Barnett, M.R., 2007. Twinning and the ductility of magnesium alloys. Part I: tension twins. *Mater. Sci. Eng. A* 464, 1–7.
- Beausir, B., Toth, L.S., Qods, F., Neale, K.W., 2009. Texture and mechanical behavior of magnesium during free-end torsion. *J. Eng. Mater. Technol.* 131, 1–15.
- Billington, E., 1977a. Non-linear mechanical response of various metals: I dynamic and static response to simple compression, tension and torsion in the as received and annealed states. *J. Phys. D* 10, 519–531.
- Billington, E., 1977b. Non-linear mechanical response of various metals: II permanent length changes in twisted tubes. *J. Phys. D* 10, 533–552.
- Billington, E., 1977c. Non-linear mechanical response of various metals: III swift effect considered in relation to the stress–strain behaviour in simple compression, tension and torsion. *J. Phys. D* 10, 553–569.
- Biswas, S., Beausir, B., Toth, L.S., Suwas, S., 2013. Evolution of texture and microstructure during hot torsion of a magnesium alloy. *Acta Materialia* 61, 5263–5277.
- Cazacu, O., Plunkett, B., Barlat, F., 2006. Orthotropic yield criterion for hexagonal closed packed materials. *Int. J. Plast.* 22, 1171–1194.
- Cazacu, O., Revil-Baudard, B., Barlat, F., 2013. New interpretation of monotonic swift effects: role of tension–compression asymmetry. *Mech. Mater.* 57, 42–52.
- Cazacu, O., Revil-Baudard, B., Barlat, F., 2014. New interpretation of cyclic Swift effects. *European Journal of Mechanics - A/Solids* 44, 82–90.
- Duchene, L., Houdaigui, F.E., Habraken, A.M., 2007. Length changes and texture prediction during free-end torsion test of copper bars with FEM and remeshing techniques. *Int. J. Plast.* 19, 1417–1438.
- Green, A.E., Naghdi, P.M., 1965. A general theory of an elastic–plastic continuum. *Arch. Ration. Mech. Anal.* 18, 251–281.
- Guo, X.Q., Wu, W., Wu, P.D., Qiao, H., An, K., Liaw, P.K., 2013. On the swift effect and twinning in a rolled magnesium alloy under free-end torsion. *Scr. Mater.* 69, 319–322.
- Habraken, A.M., Duchene, L., 2004. Anisotropic elasto-plastic finite element analysis using a stress–strain interpolation method based on a polycrystalline model. *Int. J. Plast.* 20, 1525–1560.
- Hill, R., 1948. A theory of the yielding and plastic flow of anisotropic materials. *Proc. R. Soc. London A* 193, 281–297.
- Hill, R., 1950. The mathematical theory of plasticity. Oxford University Press.
- Holtom, S.S., Kyriakides, S., Ravi-Chandar, K., 2013. Ductile failure under combined shear and tension. *Int. J. Solids Struct.* 50, 1507–1522.
- Jain, A., Agnew, S.R., 2007. Modeling the temperature dependent effect of twinning on the behavior of magnesium alloy AZ31B sheet. *Mater. Sci. Eng. A* 462, 29–36.
- Jiang, L., Jonas, J.J., Boyle, K., Martin, P., 2008. Deformation behavior of two Mg alloys during ring hoop tension testing. *Mater. Sci. Eng. A* 492, 68–73.
- Khan, A., Pandey, A., Gnaupel-Herold, T., Mishra, R.K., 2011. Mechanical response and texture evolution of AZ31 alloy at large strains for different strain rates and temperatures. *Int. J. Plast.* 27, 688–706.
- Kuroda, M., 1999. Interpretation of the behavior of metals under large plastic shear deformations: comparison of macroscopic predictions to physically based predictions. *Int. J. Plasticity* 15, 1217–1236.
- Lebensohn, R.A., Tome, C.N., 1993. A self-consistent anisotropic approach for the simulation of plastic deformation and texture development of polycrystals: application to zirconium alloys. *Acta Metall. Mater.* 41, 2611–2624.
- Lou, X.Y., Li, M., Boger, R.K., Agnew, S.R., Wagoner, R.H., 2007. Hardening evolution of AZ31B Mg sheet. *Int. J. Plast.* 23, 44–86.
- Proust, G., Tomé, C.N., Jain, A., Agnew, S.R., 2009. Modeling the effect of twinning and detwinning during strain-path changes of magnesium alloy AZ31. *Int. J. Plast.* 25, 861–880.
- Revil-Baudard, B., Chandola, N., Cazacu, O., Barlat, F., 2014. Correlation between swift effects and tension–compression asymmetry in various polycrystalline materials. *J. Mech. Phys. Solids* 70, 104–115.
- Scutti, J.J., 2001. Flowformed titanium tubular products. *Advanced Materials and Processes* 159, 69–70.
- Swift, H., 1947. Length changes in metals under torsional overstrain. *Engineering* 163, 253–257.
- Tomé, C.N., Lebensohn, R., 2004. Self-consistent homogenization methods for texture and anisotropy. In: Raabe, D., Roters, F., Barlat, F., Chen, L.-Q. (Eds.), *Continuum Scale Simulation of Engineering Materials: Fundamentals, Microstructures, Process Applications*. Wiley, New York, pp. 352–378.
- Tomé, C.N., Lebensohn, R.A., Kocks, U.F., 1991. A model for texture development dominated by deformation twinning: application to Zirconium alloys. *Acta Metall. Mater.* 39, 2667–2680.
- Toth, L.S., Jonas, J.J., Gilormini, P., Bacroix, B., 1990. Length changes during free end torsion: a rate sensitive analysis. *Int. J. Plast.* 6, 83–108.
- Van-Houtte, P., 1978. Simulation of the rolling and shear texture of brass by the Taylor theory adapted for mechanical twinning. *Acta Metall.* 26, 591–604.
- Wang, H., Raeisinia, B., Wu, P.D., Agnew, S.R., Tomé, C.N., 2010. Evaluation of self-consistent polycrystal plasticity models for magnesium alloy AZ31B sheet. *Int. J. Solids Struct.* 47, 2905–2917.